Title	Development of Co-Cr-Mo-Fe-Mn-W and Co-Cr-Mo-Fe-Mn-W-Ag high-entropy alloys based on Co-Cr-Mo alloys
Author(s)	Nagase, Takeshi; Todai, Mitsuharu; Nakano, Takayoshi
Citation	Materials Transactions. 2020, 61(4), p. 567-576
Version Type	VoR
URL	https://hdl.handle.net/11094/89895
rights	
Note	

Development of Co–Cr–Mo–Fe–Mn–W and Co–Cr–Mo–Fe–Mn–W–Ag High-Entropy Alloys Based on Co–Cr–Mo Alloys

Takeshi Nagase[1,2], Mitsuharu Todai[3] and Takayoshi Nakano[1,*]

[1]*Research Center for Ultra-High Voltage Electron Microscopy, Osaka University, Ibaraki 567-0047, Japan*
[2]*Division of Materials and Manufacturing Science, Graduate School of Engineering, Osaka University, Suita 565-0871, Japan*
[3]*Department of Environmental Materials Engineering, National Institute of Technology, Niihama College, Niihama 792-8580, Japan*

Co–Cr– and Co–Cr–Mo-based alloys are commercially used in the industry especially for high wear resistance and superior chemical and corrosion performance in hostile environments. These alloys were widely recognized as the important metallic biomaterials. Here, the first development of Co–Cr–Mo–Fe–Mn–W and Co–Cr–Mo–Fe–Mn–W–Ag high-entropy alloys (HEAs) based on Co–Cr–Mo metallic biomaterials is reported. Ingots of six-component $Co_{2.6}Cr_{1.2}Mo_{0.2}FeMnW_{0.27}$ ($Co_{41.5}Cr_{19.1}Mo_{3.2}Fe_{16}Mn_{16}W_{4.3}$, at%) HEAs with a minor σ phase and of seven-component $Co_{4.225}Cr_{1.95}Mo_{0.2}FeMnW_{0.2}Ag_{0.5}$ ($Co_{46.6}Cr_{21.5}Mo_{2.2}Fe_{11}Mn_{11}W_{2.2}Ag_{5.5}$, at%) and $Co_{2.6}Cr_{1.2}Mo_{0.1}FeMnW_{0.1}Ag_{0.18}$ ($Co_{42.1}Cr_{19.4}Mo_{1.6}Fe_{16.2}Mn_{16.2}W_{1.6}Ag_{2.9}$, at%) HEAs without an σ phase were fabricated. The alloy was designed by a taxonomy of HEAs based on the periodic table, a treelike diagram, predicted phase diagrams constructed by Materials Project, and empirical alloy parameters for HEAs. The σ phase formation prevented the formation of solid solutions in Co–Cr–Mo-based HEAs without a Ni element. The σ phase formation in as-cast ingots was discussed based on the composition dependence and valence electron concentration theory.
[doi:10.2320/matertrans.MT-MK2019002]

1. Introduction

A new class of structural and functional materials, high-entropy alloys (HEAs), has been widely investigated.[1–14] Based on the entropy-based definition of HEAs using the mixing entropy (configurational entropy) of the ideal solution and regular solution,[8,9] alloys with mixing entropy $\Delta S_{mix} \geq 1.5R$ (R is the gas constant) were classified as HEAs. ΔS_{mix} is expressed as follows.

$$\Delta S_{mix} = -R \sum_{i=1}^{n} x_i ln x_i \quad (1)$$

$$\Delta S_{mix} \geq 1.5R \text{ (HEA)} \quad (2)$$

where R is the gas constant and x_i is the mole fraction of the i-th element. Based on the entropy-based definition, medium-entropy alloys (MEAs) and low-entropy alloys (LEAs) were defined as follows:

$$1.0R \leq \Delta S_{mix} \leq 1.5R \text{ (MEA)} \quad (3)$$

$$\Delta S_{mix} \leq 1.0R \text{ (LEA)} \quad (4)$$

Table 1 shows the values of ΔS_{mix} in equiatomic CoCr, equiatomic CoCrMo, and typical Co–Cr-based and Co–Cr–Mo-based metallic biomaterials, as a typical example of the classification of alloys based on the mixing entropy. Commercial Co–Cr-based and Co–Cr–Mo-based metallic biomaterials are multicomponent alloys; however, ΔS_{mix} of these alloys was below $1.5R$.

Some preliminary attempts toward the application of HEAs for metallic biomaterials have been reported. In subsequent discussions herein, HEAs for metallic biomaterials are called "bio-HEAs." Various Ti–Nb–Ta–Zr–Mo bio-HEAs have been developed, such as equiatomic TiNbTaZrMo HEAs,[15–19] nonequiatomic $Ti_{2.6}NbTaZrMo$,[17] and $Ti_{1.4}Zr_{1.4}Nb_{0.6}Ta_{0.6}Zr_{0.6}$, $Ti_{1.7}NbTaZrMo_{0.5}$, and $Ti_{1.5}NbTaZrMo_{0.5}$ HEAs.[18] Wang *et al.* examined the application of

Table 1 ΔS_{mix} values of equiatomic CoCr, equiatomic CoCrMo, and typical Co–Cr-based and Co–Cr–Mo-based metallic biomaterials.

Alloys	ΔS_{mix} / R	LEA	MEA	HEA
Equiatomic CoCr	0.69	●		
Equiatomic CoCrMo	1.10		●	
ASTM F75 (Co-Cr-Mo)	0.74	●		
ASTM F90 (Co-Cr-W-Ni)	1.05		●	
ASTM F562 (Co-Cr-Mo-Ni)	1.23		●	
ASTM F563 (Co-Cr-Mo-Ni-Fe-W)	1.22		●	

the TiNbTaZrMo bio-HEA to orthopedic implants.[19] Yuan *et al.* reported the structure and properties of biocompatible $TiZrHfNb_xTa_x$ ($x = 0.4, 0.5, 0.6, 0.8$) bio-HEAs and bio-MEAs, including the alloy design for a low Young's modulus.[20] Motallebzadeh *et al.* reported the microstructural, mechanical, and electrochemical characterization of TiZrHfNbTa and $Ti_{1.5}ZrTa_{0.5}Hf_{0.5}Nb_{0.5}$ bio-HEAs for biomedical applications.[21] Popescu *et al.* developed TiZrNbTaFe bio-HEAs for medical applications.[22] $TiZrHfCr_{0.2}Mo$ and $TiZrHfCo_{0.06}Cr_{0.06}Mo$ bio-HEAs were developed as low-melting-temperature-type bio-HEAs whose liquidus temperature was estimated to be lower than 2000 K.[23] TiNbTaZr MEAs without toxic elements have been reported to show a strong body-centered-cubic (BCC) solid solution formation tendency and superior ductility.[15,24] The constituent elements of above-described bio-HEAs reported to date are similar to those of refractory HEAs (RHEAs).[25–31] The main and fundamental constituent elements of the above-described bio-HEAs were group IV elements of Ti and Zr and group V elements of Nb and Ta.

Co–Cr-based and Co–Cr–Mo-based alloys are commercially used in the industry; for example, Stellite is a range of Co–Cr alloys designed for high wear resistance and superior

chemical and corrosion performance in hostile environments.[32] Co–Cr-based and Co–Cr–Mo-based alloys were also recognized as one of the most important materials for metallic biomaterials together with stainless steel, pure-Ti and Ti alloys. In fact, Co–Cr-based and Co–Cr–Mo-based alloys have been commercially used as metallic biomaterials for the past 20 years,[33–39] particularly for surgical implants, such as ASTM F753,[40] ASTM F1537,[41] and JIS T 7402[42] alloys.

Despite the commercial usage of Co–Cr–Mo alloys as metallic biomaterials, no studies have attempted to develop Co–Cr–Mo-based bio-HEAs whose (Co+Cr+Mo) ratio was above 50%. In the present work, the alloy design and the development of Co–Cr–Mo–Fe–Mn–W and Co–Cr–Mo–Fe–Mn–W–Ag HEAs based on Co–Cr–Mo metallic biomaterials are reported.

2. Alloy Design

The ternary Co–Cr–Mo alloy was the starting alloy system of the bio-HEAs. Based on the taxonomy of HEAs,[11] the combination of Co, Cr, and Mo was considered inappropriate for solid solution formation compared with CoCrFeMnNi[1] as the typical 3d transition metal HEA (3d-HEA) and HfNbTaTiZr[28,29] as the typical RHEA. Figure 1 shows part of the periodic table and the main constituent elements of RHEAs and 3d-HEAs. RHEAs were designed using group IV elements (Ti, Zr, Hf), group V elements (V, Nb, Ta), and group VI elements (Cr, Mo, W). The main constituent elements of the 3d-HEAs were Cr, Mn, Fe, Co, Ni, and Cu. Cr was a constituent element of both the RHEA and 3d-HEAs. The combination of Co–Cr–Mo implies a mixture of the constituent elements of the RHEAs (Cr and Mo) and 3d-HEAs (Cr and Co); such a combination has not been commonly investigated in HEAs.[8,9] In fact, the formation of the σ phase has been reported in various HEAs whose constituent elements were a mixture of Mo (RHEA group) and Cr, Mn, Fe, Co, Ni, and Cu (3d-HEA group): AlCoCr$_x$FeMo$_{0.5}$Ni ($x = 0, 0.5, 1.0, 1.5, 2.0$),[43] Co$_{1.5}$CrFeMo$_xNi_{1.5}Ti_{0.5}$ ($x = 0.5, 0.8$),[44] AlCo$_x$CrFeMo$_{0.5}$Ni ($x = 1.5, 2.0$),[44] and AlCoCrFe$_{1.5}$Mo$_{0.5}$Ni.[44]

A parametric approach is applicable for the rough design of HEAs. The parametric approach was applied for the alloy design of Ti–Nb–Ta–Zr–Mo bio-HEAs.[15–18] In the present study, the alloy system and alloy compositions of Co–Cr–Mo-based HEAs were examined based on the empirical alloy parameters, including the following empirical parameters: mixing entropy ΔS_{mix},[8,9] mixing enthalpy ΔH_{mix},[8,9] a

parameter for evaluating the difference in the atomic radii of the constituent elements, δ,[8,9] and a dimensionless parameter Ω, which was calculated using both ΔS_{mix} and ΔH_{mix}.[8,9,44] The mixing enthalpy of the i–j atomic pair $\Delta H_{i–j}$ the atomic radii of the i elements r_i are important parameters for calculating ΔH_{mix}, δ, and Ω. The values of $\Delta H_{i–j}$ and r_i were obtained from the Takeuchi's literature.[45] ΔH_{mix}, Ω, and δ are expressed by the following equations.

$$\Delta H_{mix} = \sum_{i=1}^{n} \sum_{j \neq i}^{n} 4 \Delta H_{ij} x_i x_j \tag{5}$$

$$\Omega = \frac{T_m \cdot \Delta S_{mix}}{|\Delta H_{mix}|} \tag{6}$$

$$\delta = 100 \times \sqrt{\sum_{i=1}^{n} x_i \left(1 - \frac{r_i}{\bar{r}}\right)} \tag{7}$$

where T_m and $\bar{r}$ are the average melting temperature and average atomic radii, respectively.

The alloy design of Co–Cr–Mo-based HEAs was performed based on the treelike diagram (Fig. 2) and parametric approach (Fig. 3) using the empirical alloy parameters of ΔS_{mix}, ΔH_{mix}, $\delta(\Delta H_{\text{mix}})$, δ, and Ω. The phase diagrams predicted using Materials Project[42,43] (Fig. 4) were also used. Figure 2 shows the design of the Co–Cr–Mo-based HEAs using the treelike diagram. The following strategy was adopted to select the constituent elements. (1) Co–Cr–Mo alloys were selected as the starting alloy system (Fig. 2(a)). (2) The total amount of Co–Cr–Mo elements in HEAs was more than 50% (at%) in the design of the Co–Cr–Mo-based HEAs. (3) Alloys with $\Delta S_{\text{mix}} \geq 1.5R$ were designed for
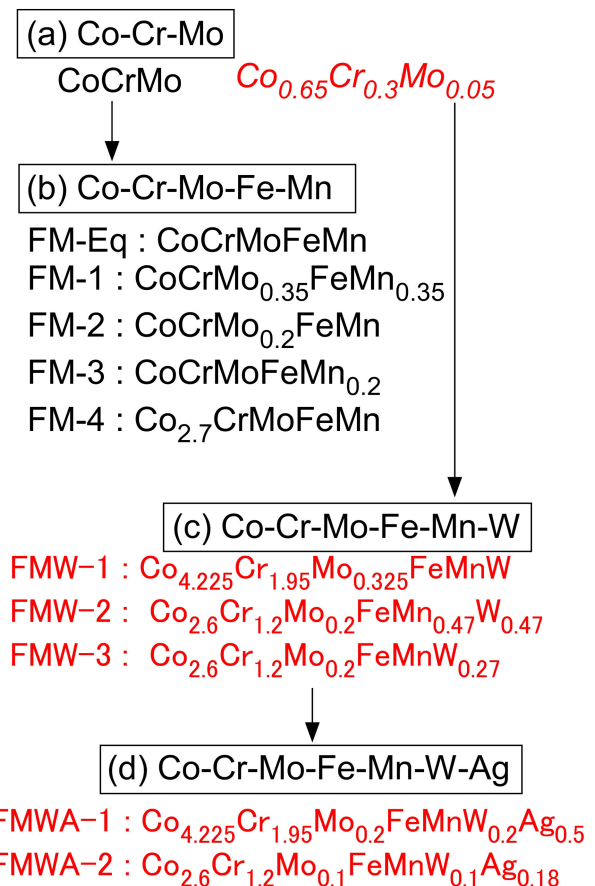

Fig. 1 Part of periodic table focusing on the constituent elements of RHEAs and 3d-HEAs.

Fig. 2 Treelike diagram for the alloy design of Co–Cr–Mo-based HEAs.

(a) ΔH_{mix}, [kJ/mol]

	Co	Cr	Mo	Fe	Mn	W	Ag
Co		−4	−5	−4	5	−1	19
Cr			−6	−1	2	1	27
Mo				−2	5	0	37
Fe					0	0	28
Mn						6	13
W							43
Ag							

(b) r [nm]

Co	0.125
Cr	0.125
Mo	0.136
Fe	0.124
Mn	0.112
W	0.137
Ag	0.144

(c) T_m [K]

Co	1768
Cr	2180
Mo	2896
Fe	1811
Mn	1519
W	3695
Ag	1235

Fig. 3　(a) Mixing enthalpy ΔH_{i-j} for i–j atomic pairs, (b) atomic radii of the i elements r_i, and (c) melting temperature of the i elements $(T_m)_i$: the data for ΔH_{i-j} and r_i were obtained from Takeuchi's literature.[45]
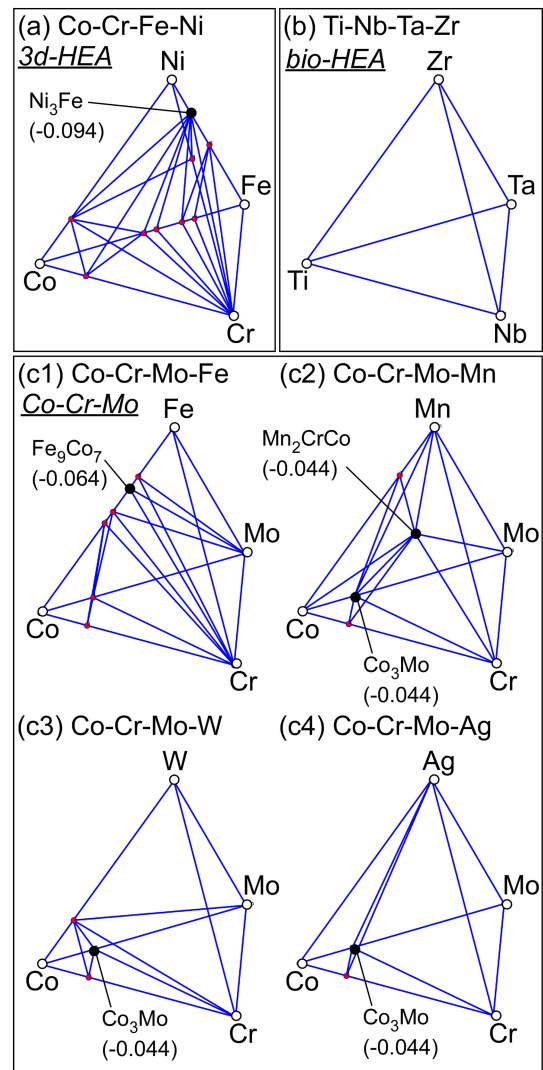

Fig. 4　Predicted phase diagram of quaternary alloy system constructed by Materials Project:[44,45] (a) Co–Cr–Fe–Ni alloy system as the typical system of 3d-HEAs, (b) Ti–Nb–Ta–Zr alloy system as the typical system of bio-HEAs, and (c) quaternary alloy systems as the typical system of Co–Cr–Mo-based HEAs, (c1) Co–Cr–Mo–Fe, (c2) Co–Cr–Mo–Mn, (c3) Co–Cr–Mo–W, and (c4) Co–Cr–Mo–Ag.

satisfying the entropy-based definitions of HEAs.[8,9] (4) Based on the parametric approach for using the empirical alloy parameters, low absolute values of ΔH_{mix} ($-20 \leq \Delta H_{mix} \leq 5$) and δ ($\delta \leq 6.6$) and a high value of Ω ($\Omega \leq 1.1$) were considered to be favorable for solid solution formation based on a previous report for the development of Ti–Nb–Ta–Zr–Mo bio-HEAs by the parametric approach.[15] To obtain optimum ΔH_{mix}, δ, and Ω, the selection of elements with low ΔH_{i-j} for Co, Cr, and Mo, and those with a similar value of r_i compared with Co, Cr, and Mo, was considered to be favorable. Fe was considered a suitable element based on Fig. 3; the absolute value of ΔH_{i-j} (i = Co, Cr, or Mo, j = Fe) was below 5 [kJ/mol], and r_{Fe} was similar to r_{Co} and r_{Cr}. Mn was also considered to be a suitable element because of the low absolute value of ΔH_{i-j} (i = Co, Cr, or Mo, j = Mn). The addition of Fe and Mn to the Co–Cr–Mo alloy system results in the formation of the Co–Cr–Mo–Fe–Mn alloy system (Fig. 2(b)). (5) The absolute values of ΔH_{i-j} (i = Co, Cr, or Mo, j = W) were near zero, and those of ΔH_{i-j} (i = Fe or Mn, j = W) were also low (Fig. 3(a)). r_W was similar to r_{Mo} (Fig. 3(b)). Despite the significantly high T_m of W (Fig. 3(c)), which makes fabrication of the ingots difficult via melting and casting, W was selected as the candidate additional element for Co–Cr–Mo-based HEAs. The Co–Cr–Mo–Fe–Mn–W alloy system was designed as shown in Fig. 2(c). (6) Ag was the particular element whose ΔH_{i-j} (i = Co, Cr, Mo, Fe, Mn, or W, j = Ag) had large positive values, indicating the low possibility of the formation of Ag-related intermetallic compounds in the

Co–Cr–Mo–Fe–Mn–W–Ag alloy system. Ag was selected as the minor element for Co–Cr–Mo-based HEAs, resulting in the Co–Cr–Mo–Fe–Mn–W–Ag alloy system, as shown in Fig. 2(d).

The additional elements for the alloy design of the Co–Cr–Mo-based HEAs were discussed based on the predicted phase diagrams constructed by Materials Project[46,47] in the present study. The predicted phase diagrams constructed by Materials Project were effective to discuss the formation of ordered-structure and/or intermetallic compounds in CoCrCuFeNi HEAs[48] and multicomponent immiscible alloys, such as Fe–Cu–Nb–B,[49] Fe–Cu–Si–B,[50] Fe–Cu–Zr–B,[50] Fe–Ag–Si–B,[51] Co–Cu–Zr–B,[52] Al–Co–La–Pb,[53] and Cu–Ag–La–Fe.[54] Based on the research works for the application of Materials Project,[48–54] an attempt was made to study the addition of Fe, Mn, W, and Ag to the Co–Cr–Mo alloy system. Figure 4 shows the predicted phase diagram of the quaternary alloy system constructed by Materials Project. Figure 4(a) shows the Co–Cr–Fe–Ni alloy system for the

typical alloy system of 3d-HEAs, such as CoCrFeMnNi.[1] Various ordered structures and/or intermetallic compounds were observed, as indicated by the red and black circles in Fig. 4(a), where the compound with the largest negative formation energy was $L1_2$-type Ni_3Fe (−0.094 eV).[55] This indicates the tendency of face-centered-cubic (FCC)-based ordering structure formation in CoCrFeNi alloys. The appearance of $L1_2$-based ordering was actually reported in CoCrMnNi MEAs.[56] Figure 4(b) shows the Ti–Nb–Ta–Zr alloy system for the typical alloy system of bio-HEAs, such as TiNbTaZrMo.[26–30] No appearance of the ordered structures and intermetallic compounds was observed in the Ti–Nb–Ta–Zr alloy system, indicating a tendency for the formation of immiscible alloys. The possibility of the decomposition of the BCC phase was examined in TiNbTaZr MEAs based on the thermodynamic calculation.[27] Figures 4(c1)–4(c4) show the Co–Cr–Mo-based quaternary alloy systems as the typical system of Co–Cr–Mo-based HEAs. The intermetallic compounds were observed in the Co–Cr–Mo–X $(X = Fe, Mn, W, Ag)$ alloy system. The compounds with the highest negative formation energy were Fe_9Co_7 (−0.064 eV)[57] in Co–Cr–Mo–Fe (Fig. 4(c1)); Mn_2CrCo (−0.044 eV),[58] and $D0_{19}$-Co_3Mo (−0.044 eV)[59] in Co–Cr–Mo–Mn (Fig. 4(c2)); Co_3Mo (−0.044 eV)[59] in Co–Cr–Mo–W (Fig. 4(c3)); and Co_3Mo (−0.044 eV)[59] in Co–Cr–Mo–Ag (Fig. 4(c4)). The highest negative formation energy in the compounds in the predicted phase diagram of the Co–Cr–Mo–X $(X = Fe, Mn, W, Ag)$ alloy system was significantly small (Figs. 4(c1)–4(c4)), and the absolute value was smaller than that of Fe_9Co_7 (−0.064 eV)[59] in Co–Cr–Mo–Fe (Fig. 4(c1)). This implies that the compound formation tendency in the Co–Cr–Mo–X $(X = Fe, Mn, W, Ag)$ alloy system was not so high and that Co–Cr–Mo-based HEAs with X $(X = Fe, Mn, W, Ag)$ elements were considered to be feasible. Based on the parametric approach (Fig. 3) and the predicted phase diagrams constructed by Materials Project (Fig. 4), the alloy systems of five-component Co–Cr–Mo–Fe–Mn (Fig. 2(b)), six-component Co–Cr–Mo–Fe–Mn–W (Fig. 2(c)), and seven-component Co–Cr–Mo–Fe–Mn–W–Ag (Fig. 2(d)) were designed.

As a five-component Co–Cr–Mo–Fe–Mn HEA, equiatomic CoCrMoFeMn HEA (FM-Eq in Fig. 2(b)) was designed as the starting alloy. Among Co, Cr, Mo, Fe, and Mn, the atomic radius of Mo (r_{Mo}) was largest, and that of Mn (r_{Mn}) was smallest (Fig. 3(b)), enabling the design of a $CoCrMo_{x1}FeMn_{x1}$ alloy $(x1 \leq 1)$. To achieve the condition $\Delta S_{mix} \geq 1.5R$, $x1 = 0.35$ was selected, resulting in a $CoCrMo_{0.35}FeMn_{0.35}$ HEA (FM-1 in Fig. 2(b)). $CoCrMo_{x2}FeMn$ alloy $(x2 \leq 1)$ and $CoCrMoFeMn_{x3}$ alloy $(x3 \leq 1)$ were considered to suppress the δ parameter related to the difference in the atomic radius of the constituent elements. Moreover, $x2 = x3 = 0.2$ was designed, resulting in $CoCrMo_{0.2}FeMn$ (FM-2 in Fig. 2(b)) and $CoCrMoFeMn_{0.2}$ (FM-3 in Fig. 2(b)) HEAs. A $Co_{x4}CrMoFeMn$ alloy $(x4 \geq 1)$ was designed, because previously developed Co–Cr–Mo-based metallic biomaterials were Co-rich alloys, such as ASTM F75.[40] To achieve the condition $\Delta S_{mix} \geq 1.5R$, $x4 = 2.7$ was selected, resulting in a $Co_{2.7}CrMoFeMn$ HEA (FM-4 in Fig. 2(b)). The alloy design that started from equiatomic CoCrMoFeMn HEA (FM-Eq in Fig. 2(b)) was not considered to be effective

for developing Co–Cr–Mo-based HEAs because of σ phase formation in the ingots. For developing six-component Co–Cr–Mo–Fe–Mn–W-based and seven-component Co–Cr–Mo–Fe–Mn–W–Ag-based HEAs, the starting alloy selected was not equiatomic CoCrMo but $Co_{0.65}Cr_{0.3}Mo_{0.05}$, whose composition was similar to ASTM F75.[40] As an alloy whose atomic ratios of Fe, Mn, and W are the same, $(Co_{0.65}Cr_{0.3}Mo_{0.05})_{y1}FeMnW$ $(y1 = 6.5)$ was designed, resulting in $Co_{4.225}Cr_{1.95}Mo_{0.325}FeMnW$ HEA (FMW-1 in Fig. 2(c)). Among Co, Cr, Mo, Fe, Mn, and W, the atomic radius of W (r_W) was largest, and that of Mn (r_{Mn}) was smallest (Fig. 3(b)), resulting in the design of $(Co_{0.65}Cr_{0.3}Mo_{0.05})_{y2}FeMn_{z2}W_{z2}$ alloy. To achieve the condition of $\Delta S_{mix} \geq 1.5R$, $y2 = 4.0$ and $z2 = 0.47$ were selected, resulting in $Co_{2.6}Cr_{1.2}Mo_{0.2}FeMn_{0.47}W_{0.47}$ HEA (FMW-2 in Fig. 2(c)). The T_m of W was much larger than that of other constituent elements in the Co–Cr–Mo–Fe–Mn–W alloy system (Fig. 3(c)). To suppress the concentration of W, $(Co_{0.65}Cr_{0.3}Mo_{0.05})_{y3}FeMnW_{z3}$ alloy was designed, resulting in $Co_{2.6}Cr_{1.2}Mo_{0.2}FeMnW_{0.27}$ HEA at $y3 = 4$ and $z3 = 0.27$ (FMW-3 in Fig. 2(c)). As denoted in the latter part (Fig. 6), the σ phase in the Co–Cr–Mo–Fe–Mn–W alloys shows the tendency to be enriched in Mo and W. To decrease the Mo and W concentration from Co–Cr–Mo–Fe–Mn–W alloys, seven-component Co–Cr–Mo–Fe–Mn–W–Ag alloys were considered. The $Co_{4.225}Cr_{1.95}Mo_{0.2}FeMnW_{0.2}Ag_{0.5}$ HEA (FMWA-1 in Fig. 2(d)) was designed from $Co_{4.225}Cr_{1.95}Mo_{0.325}FeMnW$ HEA (FMW-1 in Fig. 2(c)) to decrease the atomic ratios of Mo (FMW-1, $0.325 \to$ FMWA-1, 0.2) and W (FMW-1, $1 \to$ FMWA-2, 0.2). The $Co_{2.6}Cr_{1.2}Mo_{0.1}FeMnW_{0.1}Ag_{0.18}$ HEA (FMWA-2 in Fig. 2(d)) was designed from $Co_{2.6}Cr_{1.2}Mo_{0.2}FeMnW_{0.27}$ HEA (FMW-3 in Fig. 2(c)) to decrease the atomic ratios of Mo (FMW-3, $0.2 \to$ FMWA-2, 0.1) and W (FMW-3, $0.27 \to$ FMWA-2, 0.18). The alloy compositions and (Co+Cr+Mo) ratio are summarized in Table 2. The (Co+Cr+Mo) ratio of all alloys in Table 2 (five-component Co–Cr–Mo–Fe–Mn alloys of FM-X_1 $(X_1 = Eq, 1, 2, 3, 4)$, six-component Co–Cr–Mo–Fe–Mn–W alloys of FMW-X_2 $(X_2 = 1, 2, 3)$, and seven-component Co–Cr–Mo–Fe–Mn–W–Ag alloys of FMWA-X_3 $(X_3 = 1, 2)$) was more than 50%, and most alloys were above 60%.

Table 3 summarizes the empirical alloy parameters of ΔS_{mix}, ΔH_{mix}, δ, and Ω, together with the $\delta(\Delta H_{mix})$ parameter.[60] The alloys with low absolute value of $\delta(\Delta H_{mix})$ have the tendency to show the solid solution phase without the difficulty in the fabrication of the ingots via casting process. Among alloys in Table 3, the δ value of the alloy $Co_{4.225}Cr_{1.95}Mo_{0.2}FeMnW_{0.2}Ag_{0.5}$ (FMWA-1) was not satisfied with the condition $\delta \leq 6.6$; however, the absolute value of ΔH_{mix} was nearly zero, and it had the largest Ω value among the alloys in Table 3. The empirical alloy parameters of the other alloys were satisfied with the conditions of ΔH_{mix} $(-20 \leq \Delta H_{mix} \leq 5)$, δ $(\delta \leq 6.6)$, and Ω $(\Omega \leq 1.1)$. The value of $\delta(\Delta H_{mix})$ in Co–Cr–Mo-based alloys in Table 3 was similar to those of the conventional 3d-HEAs,[1,8,9] RHEAs,[25–31] and HE brasses.[61,62] This implies the possibility that the solid solution formation in alloys in Table 3 was large from the viewpoint of the parametric approach using empirical alloy parameters.

Table 2   Alloy composition of Co–Cr–Mo-based HEAs (atomic percent).

Alloys		Composition [at%]							(Co+Cr+Mo) ratio [%]
		Co	Cr	Mo	Fe	Mn	W	Ag	
FM-Eq	CoCrMoFeMn	20.00	20.00	20.00	20.00	20.00			60.00
FM-1	$CoCrMo_{0.35}FeMn_{0.35}$	27.03	27.03	9.46	27.03	9.46			63.51
FM-2	$CoCrMo_{0.2}FeMn$	23.81	23.81	4.76	23.81	23.81			52.38
FM-3	$CoCrMoFeMn_{0.2}$	23.81	23.81	23.81	23.81	4.76			71.43
FM-4	$Co_{2.7}CrMoFeMn$	40.30	14.93	14.93	14.93	14.93			70.15
FMW-1	$Co_{4.225}Cr_{1.95}Mo_{0.325}FeMnW$	44.47	20.53	3.42	10.53	10.53	10.53		68.42
FMW-2	$Co_{2.6}Cr_{1.2}Mo_{0.2}FeMn_{0.47}W_{0.47}$	43.77	20.20	3.37	16.84	7.91	7.91		67.34
FMW-3	$Co_{2.6}Cr_{1.2}Mo_{0.2}FeMnW_{0.27}$	41.47	19.14	3.19	15.95	15.95	4.31		63.80
FMWA-1	$Co_{4.225}Cr_{1.95}Mo_{0.2}FeMnW_{0.2}Ag_{0.5}$	46.56	21.49	2.20	11.02	11.02	2.20	5.51	70.25
FMWA-2	$Co_{2.6}Cr_{1.2}Mo_{0.1}FeMnW_{0.1}Ag_{0.18}$	42.07	19.42	1.62	16.18	16.18	1.62	2.91	63.11

Table 3   Empirical alloy parameters of Co–Cr–Mo-based HEAs (atomic percent).

Alloys		Alloy parameters				
		$\Delta S_{mix}/R$	ΔH_{mix} [kJ/mol]	$\delta(\Delta H_{mix})$ [kJ/mol]	δ	Ω
FM-Eq	CoCrMoFeMn	1.61	—2.2	+4.2	6.1	11.8
FM-1	$CoCrMo_{0.35}FeMn_{0.35}$	1.51	—3.5	+3.1	4.2	7.1
FM-2	$CoCrMo_{0.2}FeMn$	1.51	—2.8	+3.8	5.1	8.4
FM-3	$CoCrMoFeMn_{0.2}$	1.51	—3.5	+3.1	4.6	7.3
FM-4	$Co_{2.7}CrMoFeMn$	1.50	—4.0	+3.0	5.3	6.2
FMW-1	$Co_{4.225}Cr_{1.95}Mo_{0.325}FeMnW$	1.51	—3.2	+2.9	4.9	8.5
FMW-2	$Co_{2.6}Cr_{1.2}Mo_{0.2}FeMn_{0.47}W_{0.47}$	1.50	—3.5	+2.6	4.3	7.4
FMW-3	$Co_{2.6}Cr_{1.2}Mo_{0.2}FeMnW_{0.27}$	1.50	—3.5	+2.8	4.3	7.4
FMWA-1	$Co_{4.225}Cr_{1.95}Mo_{0.2}FeMnW_{0.2}Ag_{0.5}$	1.50	+0.95	+7.4	7.0	24.5
FMWA-2	$Co_{2.6}Cr_{1.2}Mo_{0.1}FeMnW_{0.1}Ag_{0.18}$	1.51	—1.3	+5.2	5.3	18.6

3.   Experimental Procedures and Calculation Details

Arc-melted ingots of the Co–Cr–Mo-based HEAs were prepared in an arc-melting furnace from a mixture of pure-element lumps. The total amount of the ingot was approximately 20 g. Co flakes (3N), Cr granules (3N), Mo shots (3N), Fe flakes (3N), Mn flakes (3N), W shots (3N), and Ag shots (3N) were used as pure-element lumps. To achieve homogeneous distributions of the constituent elements in the alloys, the alloy ingots were melted more than 10 times and maintained in a liquid state for approximately 120 s during each melting cycle. The cooling rate during arc-melting was approximately 2×10^3 K/s.[16,63] X-ray diffraction (XRD) analysis was performed with Cu-K$_\alpha$ radiation to identify the constituent phases. The solidification microstructures of the arc-melted ingots were investigated by scanning electron microscopy (SEM) backscattered electron (BSE) imaging and by electron probe microanalysis with wavelength-dispersive spectroscopy (EPMA-WDS). The thermodynamic calculations were performed with FactSage (ver. 7.3) using the thermodynamic databases for alloy systems from Scientific Group Thermodata Europe (SGTE) 2017.[64]

4.   Results

The main constituent phases of the arc-melted ingots of five-component Co–Cr–Mo-based Co–Cr–Mo–Fe–Mn HEAs of FM-X$_1$ (X$_1$ = Eq, 1, 2, 3, 4) was identified as σ phase by XRD patterns. Figure 5 shows XRD patterns of the arc-melted ingots of six-component Co–Cr–Mo–Fe–Mn–W HEAs of FMW-X$_2$ (X$_2$ = 1, 2, 3). XRD intensity profiles of the FCC phase in $Co_{0.239}Cr_{0.239}Fe_{0.468}$ alloy, HCP phase in $Co_{0.64}Cr_{0.32}Mo_{0.04}$ alloy, and σ phase in $Co_{0.475}Cr_{0.31}Mo_{0.215}$ alloy are shown in the bottom part of the figure.[65] In the alloys $Co_{4.225}Cr_{1.95}Mo_{0.325}FeMnW$ (FMW-1) and $Co_{2.6}Cr_{1.2}Mo_{0.2}FeMn_{0.47}W_{0.47}$ (FMW-2), the constituent phases are identified as a mixture of HCP (indicated by the black filled circle, ●) and σ phase (indicated by the open star, ☆). In contrast, the main constituent phase was identified as FCC
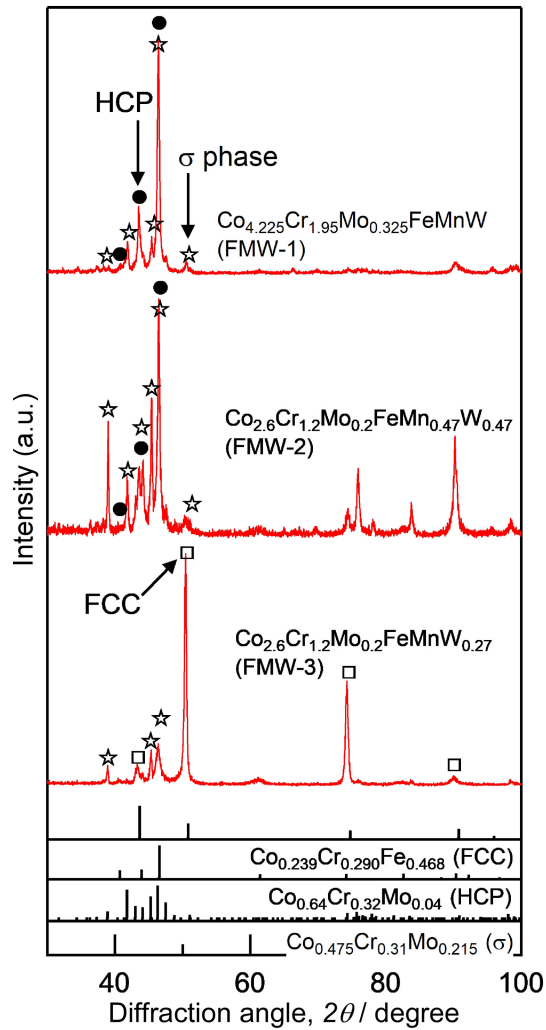
Fig. 5   XRD patterns of the arc-melted ingots of six-component Co–Cr–Mo–Fe–Mn–W HEAs: XRD intensity profiles of FCC phase in $Co_{0.239}Cr_{0.239}Fe_{0.468}$ alloy, HCP phase in $Co_{0.64}Cr_{0.32}Mo_{0.04}$ alloy, and σ phase in $Co_{0.475}Cr_{0.31}Mo_{0.215}$ alloy are shown in the bottom part of the figure.[65]
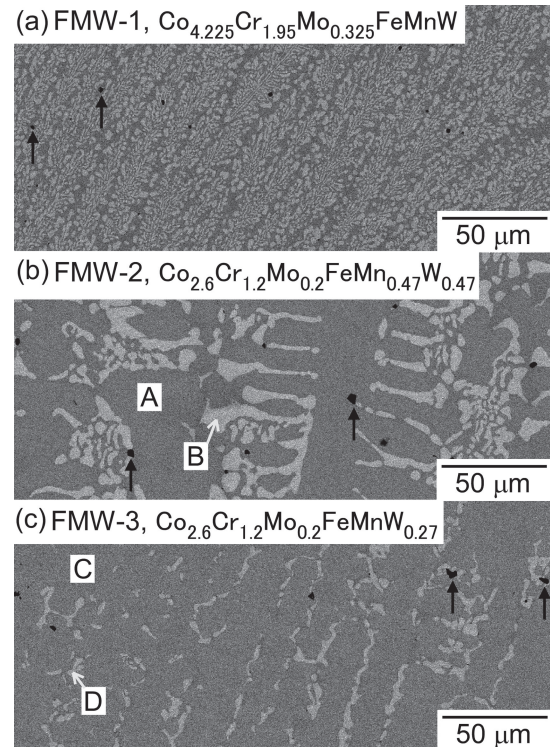

Fig. 6   SEM-BSE images of the arc-melted ingots of six-component Co–Cr–Mo–Fe–Mn–W HEAs: (a) $Co_{4.225}Cr_{1.95}Mo_{0.325}FeMnW$ (FMW-1), (b) $Co_{2.6}Cr_{1.2}Mo_{0.2}FeMn_{0.47}W_{0.47}$ (FMW-2), (c) $Co_{2.6}Cr_{1.2}Mo_{0.2}FeMnW_{0.27}$ (FMW-3), (b) HEAs: the indices A and C indicate the dendrite region with gray contrast, and the indices B and D indicate the interdendrite region with white contrast, respectively, and the black contrast regions indicated by the black arrows are polishing artifacts related to SiC from abrasive papers.

Table 4   EPMA-WDS composition analysis results of gray-contrast dendrite region (C) and white-contrast interdendrite region (D) in the arc-melted ingots of the $Co_{2.6}Cr_{1.2}Mo_{0.2}FeMnW_{0.27}$ alloy (FMW-3).

	Co	Cr	Mo	Fe	Mn	W
Dendrite (C)	44.1	19.9	2.4	17.4	14.0	2.2
Interdendrite (D)	35.3	24.2	6.7	13.3	16.3	4.1

phase (indicated by the open circle, ○) in alloy $Co_{2.6}Cr_{1.2}Mo_{0.2}FeMnW_{0.27}$ (FMW-3), where the σ phase was also observed as the minor phase.

To investigate the solidification microstructure, SEM-BSE images were obtained from the central region of the ingots. Figure 6 shows SEM-BSE images of the arc-melted ingots of six-component Co–Cr–Mo–Fe–Mn–W HEAs of FMW-X_2 ($X_2 = 1, 2, 3$). The randomly dispersed black contrast regions indicated by the black arrows were the polishing artifacts related to SiC from abrasive papers.[66] A fine eutectic-like structure was observed in alloy $Co_{4.225}Cr_{1.95}Mo_{0.325}FeMnW$ (FMW-1) (Fig. 6(a)). The gray-contrast dendrite phase (indicated by the index A) and white–gray-contrast interdendrite region (indicated by the index B) were observed in the alloy $Co_{2.6}Cr_{1.2}Mo_{0.2}FeMn_{0.47}W_{0.47}$ (FMW-2) (Fig. 6(b)). The area ratio of the white–gray-contrast interdendrite region (indicated by the index D) vs. gray-contrast dendrite region (indicated by the index C) in alloy $Co_{2.6}Cr_{1.2}Mo_{0.2}FeMnW_{0.27}$ (FMW-3) (Fig. 6(c)) was much lower than that of alloy $Co_{2.6}Cr_{1.2}Mo_{0.2}FeMn_{0.47}W_{0.47}$ (FMW-2) (A vs. B in Fig. 6(b)). Based on the XRD pattern

(Fig. 5) and SEM-BSE images (Fig. 6(c)), the gray-contrast dendrite region (C) and white–gray-contrast interdendrite region (D) were considered to correspond to the FCC phase and σ phase, respectively, in alloy $Co_{2.6}Cr_{1.2}Mo_{0.2}FeMnW_{0.27}$ (FMW-3). The quantitative composition analysis results of the dendrite (C) and interdendrite (D) regions by EPMA-WDS are shown in Table 4. The dendrite (C) and interdendrite (D) regions both contain all constituent elements. A significant difference between the atomic compositions of Fe and Mn was not observed between the dendrite (C) and interdendrite (D) regions, compared with the other elements of Co, Cr, Mo and W. The constituent phases and the solidification microstructure depended strongly on the alloy composition in six-component Co–Cr–Mo–Fe–Mn–W HEAs.

Figure 7 shows XRD patterns of the arc-melted ingots of seven-component Co–Cr–Mo–Fe–Mn–W–Ag HEAs of FMWA-X_3 ($X_3 = 1, 2$). XRD intensity profiles of the FCC phase in Ag and $Co_{0.239}Cr_{0.239}Fe_{0.468}$ alloy and HCP phase
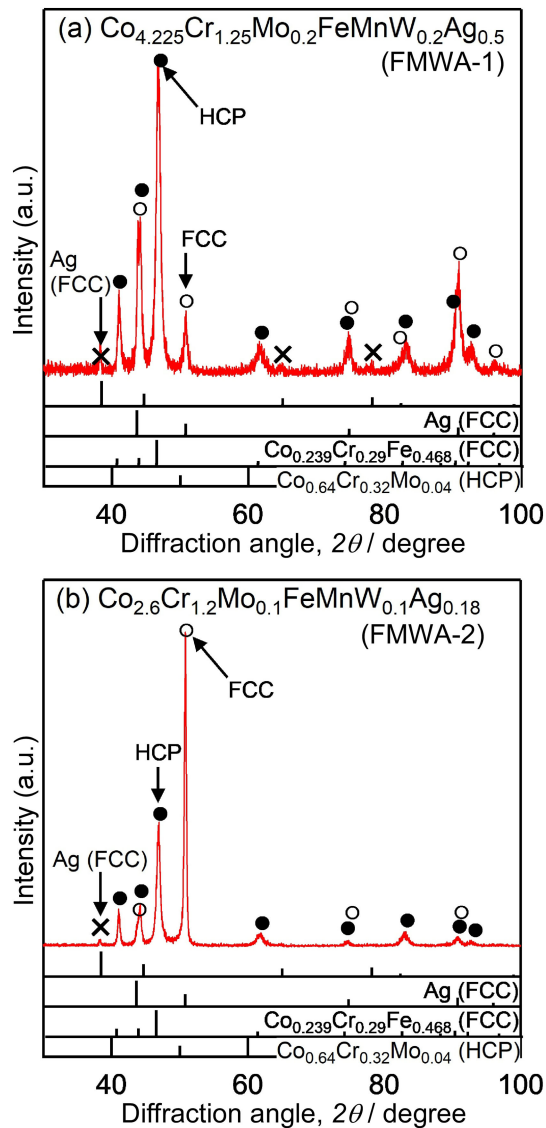
Fig. 7 XRD patterns of the arc-melted ingots of seven-component Co–Cr–Mo–Fe–Mn–W–Ag HEAs: XRD intensity profiles of FCC phase in Ag and $Co_{0.239}Cr_{0.239}Fe_{0.468}$ alloy and of HCP phase in $Co_{0.64}Cr_{0.32}Mo_{0.04}$ alloy are shown in the bottom part of the figure,[65] (a) $Co_{4.225}Cr_{1.25}Mo_{0.2}FeMnW_{0.2}Ag_{0.5}$ (FMWA-1) and (b) $Co_{2.6}Cr_{1.2}Mo_{0.1}FeMnW_{0.1}Ag_{0.18}$ (FMWA-2).
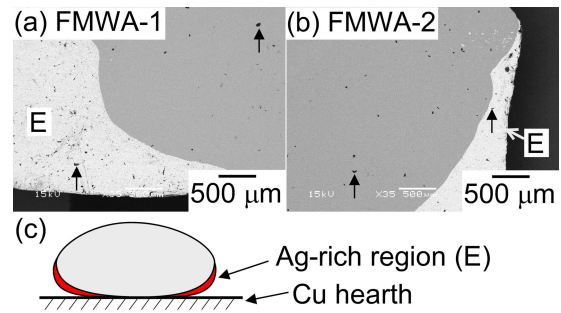

Fig. 8 SEM-BSE images of the arc-melted ingots of seven-component Co–Cr–Mo–Fe–Mn–W–Ag HEAs focusing on the minor Ag-rich region at the bottom side the ingots (a), (b), and the schematic illustration of the position of the Ag-rich region at the bottom side the ingots (c): (a) $Co_{4.225}Cr_{1.25}Mo_{0.2}FeMnW_{0.2}Ag_{0.5}$ (FMWA-1) and (b) $Co_{2.6}Cr_{1.2}Mo_{0.1}$-$FeMnW_{0.1}Ag_{0.18}$ (FMWA-2).

in $Co_{0.64}Cr_{0.32}Mo_{0.04}$ alloy are shown in the bottom part of the figure.[65] Sharp intensity peaks corresponding to σ phase were not observed in $Co_{4.225}Cr_{1.25}Mo_{0.2}FeMnW_{0.2}Ag_{0.5}$ (FMWA-1) and $Co_{2.6}Cr_{1.2}Mo_{0.2}FeMnW_{0.1}Ag_{0.18}$ (FMWA-2) HEAs. Most of the high-intensity peaks can be indexed as FCC and HCP phases, and minor peaks corresponding to the FCC-Ag phase were observed. To investigate the distribution of the FCC-Ag phase in the ingots, the solidification microstructure was investigated, and the results are shown in Fig. 8. Figures 8(a) and 8(b) show the SEM-BSE images of the arc-melted ingots of seven-component Co–Cr–Mo–Fe–Mn–W–Ag HEAs of FMWA-X₃ (X₃ = 1, 2) focusing on the minor Ag-rich region at the bottom side of the ingots. In Figs. 8(a) and 8(b), the black contrast regions (black arrows) randomly dispersed in the ingots were identified as the polishing artifacts related to the SiC from abrasive papers.[66] The existence of a macroscopically phase-separated white

contrast region (indicated by the index E) was observed at the bottom side in alloy $Co_{4.225}Cr_{1.25}Mo_{0.2}FeMnW_{0.2}Ag_{0.5}$ (FMWA-1) (Fig. 8(a)) and alloy $Co_{2.6}Cr_{1.2}Mo_{0.2}FeMn$-$W_{0.1}Ag_{0.18}$ (FMWA-2) (Fig. 8(b)). Figure 8(c) shows the schematic illustration of the position of the Ag-rich region (E) at the bottom side of the ingots. The solubility of Ag in the FCC and HCP phases was significantly small, and an Ag-rich phase with an FCC structure was formed in the ingots of seven-component Co–Cr–Mo–Fe–Mn–W–Ag HEAs.

5. Discussion

The formation of the σ phase was observed in the arc-melted ingots of various alloys designed in the present study. The suppression of σ phase formation was most vital for the development of Co–Cr–Mo-based HEAs without Ni. It was found that the σ phase formation tendency was predicted by the atomic ratio of (Mo+W), where Mo and W belonged to the constituent elements of RHEAs and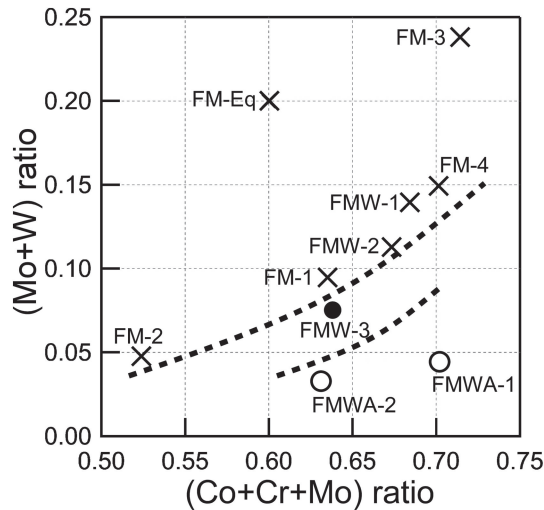 not to 3d-HEAs, as shown in Fig. 1. Figure 9 shows conditions delineating σ phase formation in the arc-melted ingots in Co–Cr–Mo-based HEAs based on the composition of the constituent element, where the X- and Y-axes correspond to the (Co+Cr+Mo) and (Mo+W) ratios, respectively. In Fig. 9, the black X-mark denotes the alloy with the main constituent phase as the σ phase, the black filled circle (●) indicates the composite of the main solid solution phase and the minor σ phase, and the black open circle (○) implies solid solution formation without the σ phase in the arc-melted ingots. The σ phase formation tended to be suppressed by the decrease in the (Mo+W) ratio. The increase in the (Co+Cr+Mo) ratio together with the decrease in the (Mo+W) ratio was considered to be effective for obtaining the solid solution phase without the σ phase.

Tsai *et al.* reported that the valence electron concentration (*VEC*) was effective to predict the σ phase formation in as-cast ingots of Cr- and V-containing HEAs;[67] the *VEC* range for the formation of the σ phase was 6.88 < *VEC* < 7.84, and no σ phase formation was found outside this range. The general applicability of the *VEC* rule to the formation of the σ phase in as-cast specimens in other alloy systems has been uncertain.[9] In the present study, an attempt was made to

Fig. 9   Conditions delineating σ phase formation in the arc-melted ingots in Co–Cr–Mo-based HEAs based on the composition of the constituent element: the X- and Y-axes correspond to the (Co+Cr+Mo) and (Mo+W) ratios, respectively.
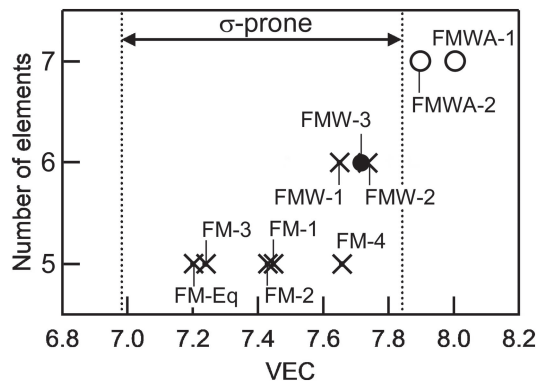

Fig. 10   Conditions delineating σ phase formation in the arc-melted ingots in Co–Cr–Mo-based HEAs based on VEC.

summarize the σ phase formation tendency in Co–Cr–Mo-based HEAs without V elements by the *VEC* rule suggested by Tsai *et al.*[67] The results are shown in Fig. 10. Figure 10 shows the relationship between *VEC* and the presence of the σ phase in as-cast ingots, where the black X-mark, the black filled circle (●), and the black open circle (○) mean the σ-prone alloys, the alloys with minor σ phase, and σ-free alloys, respectively. The σ phase formation in the present study was well predicted by Tsai's criterion for the *VEC* rules in σ phase formation. The *VEC* of Ag (*VEC* = 11) was the largest among the constituent elements of seven-component Co–Cr–Mo–Fe–Mn–W–Ag HEAs (*VEC* values: Co = 9, Cr = 6, Mo = 6, Fe = 8, Mn = 7, W = 6, and Ag = 11). The suppression of the σ phase formation by the addition of Ag corresponded to the increase of the *VEC* of alloys for *VEC* > 7.84. The increase in the (Mo+W) ratio led to a decrease of the *VEC* value in Co–Cr–Mo-based five-component Co–Cr–Mo–Fe–Mn, six-component Co–Cr–Mo–Fe–Mn–W, and seven-component Co–Cr–Mo–Fe–Mn–W–Ag HEAs, resulting in the satisfaction of the VEC range $6.88 < VEC < 7.84$ for σ phase formation. The *VEC* of Mo and W (*VEC* = 6) was lowest among Co, Cr, Mo, Fe, Mn, W and Ag. There was no discrepancy between the strong

compositional dependence of σ phase formation summarized by the (Mo+W) ratio (Fig. 9) and *VEC* rule for σ formation shown in Fig. 10. The calculation of the (Mo+W) ratio and *VEC* was significantly easy for the multicomponent alloys, and they were effective to predict the σ formation in Co–Cr–Mo-based HEAs.

Ag-rich phase formation was observed at the bottom side of the arc-melt ingots in seven-component Co–Cr–Mo–Fe–Mn–W–Ag-based HEAs of $Co_{4.225}Cr_{1.25}Mo_{0.2}FeMnW_{0.2}Ag_{0.5}$ (FMWA-1) and $Co_{2.6}Cr_{1.2}Mo_{0.2}FeMnW_{0.1}Ag_{0.18}$ (FMWA-2) (Fig. 8). The Ag-rich phase formation at the bottom side of the arc-melt ingots was also observed in Co–Cr–Fe–Mn–Ni–Ag HEAs,[68] and this was explained by the liquid-phase separation and the Ag-rich separated liquid formation. The occurrence of the liquid-phase separation and the formation of the Ag-rich region was also reported for Ag-containing Al–Co–Cr–Cu–Ni–Ag HEAs.[69] The formation of the Ag-rich region at the bottom side of the arc-melted ingots whose morphology was similar to the image in Fig. 8(c) was found in Ti–Ag immiscible alloys with liquid-phase separation.[63] The ΔH_{i-j} map (Fig. 3(a)) indicates that the ΔH_{i-j} of Ag (i = Co, Cr, Mo, Fe, Mn, W, j = Ag) and the other constituent elements had large positive values. The large positive values in ΔH_{i-j} indicate the repulsive nature between i–j pairs. The Ag element has a repulsive nature against Co, Cr, Mo, Fe, Mn, and W, indicating the strong liquid-phase separation tendency in seven-component Co–Cr–Mo–Fe–Mn–W–Ag HEAs. The thermodynamic calculation focusing only on liquid phases was effective to predict the liquid phase separation in multi-component alloys,[49–54,71–73] including the formation of Ag-rich liquid phase via liquid phase sepatation.[51,54,73] Thermodynamic calculation of the Gibbs free energy of liquid phases in seven-component Co–Cr–Mo–Fe–Mn–W–Ag HEAs focusing on the atomic ratio of Ag were performed, where the calculation details were similar to the previous literatures.[49–54,70–73] The results were shown in Fig. 11. It should be noted here that only Ag–Co binary alloys system was not assessed in the binary Ag–X (X = Co, Cr, Mo, Fe, Mn, W) alloy system in SGTE2017. Figure 11 shows the temperature dependence of the Gibbs-free-energy curves of liquid phases in $(Co_{0.421}Cr_{0.194}Mo_{0.016}Fe_{0.162}Mn_{0.162}W_{0.016})_{1-x}Ag_x$ alloys in-
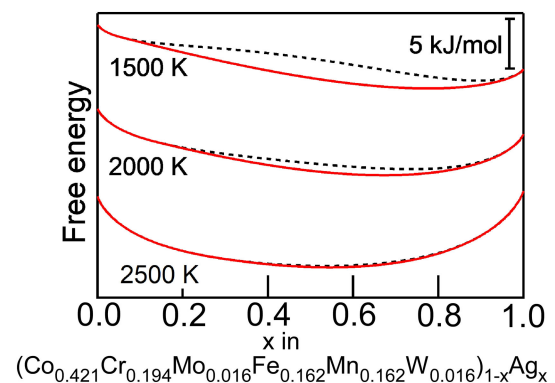

Fig. 11   Thermodynamic calculation of the Gibbs free energy of liquid phase in seven-component Co–Cr–Mo–Fe–Mn–W–Ag HEAs of $(Co_{0.421}Cr_{0.194}Mo_{0.016}Fe_{0.162}Mn_{0.162}W_{0.016})_{1-x}Ag_x$ alloys including $Co_{2.6}Cr_{1.2}Mo_{0.1}FeMnW_{0.1}Ag_{0.18}$ (x = 0.0291) (FMWA-2) focusing on the atomic ratio of Ag.
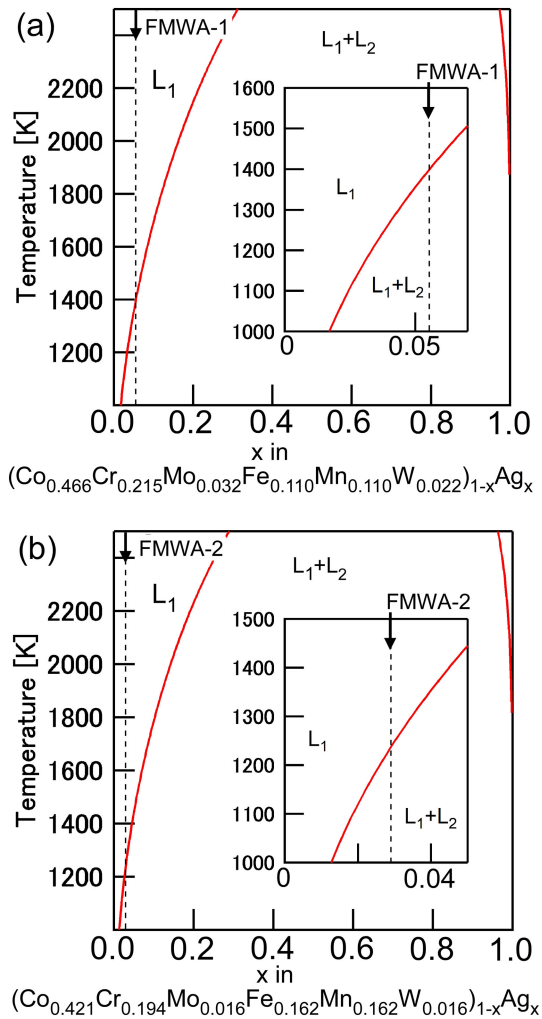
Fig. 12 Thermodynamic calculation of the liquid miscibility gap in seven-component Co–Cr–Mo–Fe–Mn–W–Ag HEAs focusing on the atomic ratio of Ag. (a) $(Co_{0.466}Cr_{0.215}Mo_{0.032}Fe_{0.11}Mn_{0.11}W_{0.022})_{1-x}Ag_x$ alloys including $Co_{4.225}Cr_{1.25}Mo_{0.2}FeMnW_{0.2}Ag_{0.5}$ ($x = 0.0551$) (FMWA-1), (b) $(Co_{0.421}Cr_{0.194}Mo_{0.016}Fe_{0.162}Mn_{0.162}W_{0.016})_{1-x}Ag_x$ alloys including $Co_{2.6}Cr_{1.2}Mo_{0.1}FeMnW_{0.1}Ag_{0.18}$ ($x = 0.0291$) (FMWA-2).

cluding $Co_{2.6}Cr_{1.2}Mo_{0.1}FeMnW_{0.1}Ag_{0.18}$ ($x = 0.0291$) (FMWA-2). The Gibbs free energy of the single-liquid phase (indicated by the black-broken line) was higher than that of two-liquid state (indicated by the red-solid line) with a wide x range in $(Co_{0.421}Cr_{0.194}Mo_{0.016}Fe_{0.162}Mn_{0.162}W_{0.016})_{1-x}Ag_x$ alloys. This indicates the occurrence of liquid-phase separation in $(Co_{0.421}Cr_{0.194}Mo_{0.016}Fe_{0.162}Mn_{0.162}W_{0.016})_{1-x}Ag_x$ alloys at temperatures at and below 2500 K. The liquid phase separation tendency was also detected in the temperature dependence of the Gibbs-free-energy curves of liquid phases in $(Co_{0.466}Cr_{0.215}Mo_{0.032}Fe_{0.11}Mn_{0.11}W_{0.022})_{1-x}Ag_x$ alloys including $Co_{4.225}Cr_{1.25}Mo_{0.2}FeMnW_{0.2}Ag_{0.5}$ ($x = 0.0551$) (FMWA-1). The liquid miscibility gap constructed by the Gibbs free energy is shown in Fig. 12. The inset in Figs. 12(a) and 12(b) shows the Co–Cr–Mo–Fe–Mn–W-rich side of the liquid miscibility gap. The mixture of the separated Co–Cr–Mo–Fe–Mn–W-rich (L_1) and Ag-rich (L_2) liquids was more stably existed than the single-liquid state with a wide x range in $(Co_{0.466}Cr_{0.215}Mo_{0.032}Fe_{0.11}Mn_{0.11}W_{0.022})_{1-x}Ag_x$ alloys including $Co_{4.225}Cr_{1.25}Mo_{0.2}FeMnW_{0.2}Ag_{0.5}$ ($x = 0.0551$) (FMWA-1) (Fig. 12(a)) and

$(Co_{0.421}Cr_{0.194}Mo_{0.016}Fe_{0.162}Mn_{0.162}W_{0.016})_{1-x}Ag_x$ alloys including $Co_{2.6}Cr_{1.2}Mo_{0.1}FeMnW_{0.1}Ag_{0.18}$ ($x = 0.0291$) (FMWA-2) (Fig. 12(b)). The formation of the Ag-rich region in the arc-melted ingots in seven-component Co–Cr–Mo–Fe–Mn–W–Ag HEAs can be explained by the liquid phase separation without any discrepancy.

The parametric approach using ΔS_{mix}, ΔH_{mix}, δ, and Ω was effective to develop Ti–Nb–Ta–Zr–Mo bio-HEAs, while the approach without any modification was not applicable for Co–Cr–Mo-based HEAs because of the σ phase formation. The σ phase formation in Co–Cr–Mo-based HEAs was predicted by the compositional map using the (Mo+W) ratio, and/or the VEC parameter. The combination of various parameters (ΔS_{mix}, ΔH_{mix}, δ, Ω, $\delta(\Delta H_{mix})$, VEC, and (Mo+W) ratio) was considered to be effective to develop Co–Cr–Mo-based HEAs. The mechanical properties and biocompatibility were not evaluated, because the present study focused on the alloy design. It is planned that these properties for metallic biomaterials will be reported in future works.

6. Conclusions

The first development of Co–Cr–Mo-based Co–Cr–Mo–Fe–Mn–W and Co–Cr–Mo–Fe–Mn–W–Ag HEAs without Ni elements is reported, where these alloys were designed based on Co–Cr–Mo-based metallic biomaterials. The obtained results and conclusions are summarized as follows.

(1) Co–Cr–Mo-based HEAs without Ni were designed by the taxonomy of HEAs based on the periodic table, a treelike diagram, a parametric approach using empirical alloy parameters for HEAs, and the predicted phase diagram constructed by Materials Project.

(2) Formation of the σ phase was observed in the arc-melted ingots of five-component Co–Cr–Mo–Fe–Mn and six-component Co–Cr–Mo–Fe–Mn–W HEAs.

(3) The ingots of six-component $Co_{2.6}Cr_{1.2}Mo_{0.2}$-$FeMnW_{0.27}$ ((Co+Cr+Mo) ratio = 0.638) HEA showed a composite of the main FCC and minor σ phase.

(4) Solid solutions without the σ phase were obtained in arc-melted ingots of seven-component $Co_{4.225}Cr_{1.95}$-$Mo_{0.2}FeMnW_{0.2}Ag_{0.5}$ ((Co+Cr+Mo) ratio = 0.703) and $Co_{2.6}Cr_{1.2}Mo_{0.1}FeMnW_{0.1}Ag_{0.18}$ ((Co+Cr+Mo) ratio = 0.631) HEAs.

(5) The composition map using the (Co+Cr+Mo) ratio and (Mo+W) ratio and/or the VEC parameter was effective for predicting the σ phase formation in the ingots of Co–Cr–Mo-based HEAs.

(6) Liquid phase separation behaviors in seven-component Co–Cr–Mo–Fe–Mn–W–Ag HEAs can be explained by the thermodynamic calculation focusing only on liquid phases.

tion Promotion Program (SIP); and the Innovative Design/ Manufacturing Technologies program (Establishment and Validation of the Base for 3D Design and Additive Manufacturing Standing on the Concepts of "Anisotropy" and "Customization") of the New Energy and Industrial Technology Development Organization (NEDO).

REFERENCES

1) B. Cantor, I.T.H. Chang, P. Knight and A.J.B. Vincent: Mater. Sci. Eng. A **375–377** (2004) 213–218.
2) J.W. Yeh, S.K. Chen, S.J. Lin, J.Y. Gan, T.S. Chin, T.T. Shun, C.H. Tsau and S.Y. Chang: Adv. Eng. Mater. **6** (2004) 299–303.
3) S. Ranganathan: Curr. Sci. **85** (2003) 1404–1406.
4) Y. Zhang, Y.J. Zhou, J.P. Lin, G.L. Chen and P.K. Liew: Adv. Eng. Mater. **10** (2008) 534–538.
5) J.W. Yeh: JOM **65** (2013) 1759–1771.
6) M.H. Tsai and J.W. Yeh: Mater. Res. Lett. **2** (2014) 107–123.
7) Y. Zhang, T.T. Zuo, Z. Tang, M.C. Gao, K.A. Dahmen, P.K. Liaw and Z.P. Lu: Prog. Mater. Sci. **61** (2014) 1–93.
8) B.S. Murty, J.-W. Yeh and S. Ranganathan: *High-Entropy Alloys*, 1st ed., (Elsevier, Amsterdam, 2014).
9) M.C. Gao, J.-W. Yeh, P.K. Liaw and Y. Zhang: *High-Entropy Alloys, Fundamentals and Applications*, 1st ed., (Springer, Berlin, 2016).
10) Y.F. Ye, Q. Wang, J. Lu, C.T. Liu and Y. Yang: Mater. Today **19** (2016) 349–362.
11) D.B. Miracle and O.N. Senkov: Acta Mater. **122** (2017) 448–511.
12) T. Nagase: J. Soc. Mech. Eng. **121**(1192) (2018) 8–11.
13) W. Zhang, P.K. Liew and Y. Zhang: Sci. China Mater. **61** (2018) 2–22.
14) D.B. Miracle: Nat. Commun. **10** (2019) 1805.
15) M. Todai, T. Nagase, T. Hori, A. Matsugaki, A. Sekita and T. Nakano: Scr. Mater. **129** (2017) 65–68.
16) T. Nagase, K. Mizuuchi and T. Nakano: Entropy **21** (2019) 483.
17) T. Nagase, M. Todai, T. Hori and T. Nakano: J. Alloy. Compd. **753** (2018) 412–421.
18) T. Hori, T. Nagase, M. Todai, A. Matsugaki and T. Nakano: Scr. Mater. **172** (2019) 83–87.
19) S.P. Wang and J. Xu: Mater. Sci. Eng. C **73** (2017) 80–89.
20) Y. Yuan, Y. Wu, Z. Yang, X. Liang, Z. Lei, H. Huang, H. Wang, X. Liu, K. An, W. Wu and Z. Lu: Mater. Res. Lett. **7** (2019) 225–231.
21) A. Motallebzadeh, N.S. Peighambardoust, S. Sheikh, H. Murakami, S. Guo and D. Canadinc: Intermetallics **113** (2019) 106572.
22) G. Popescu, B. Ghiban, C.A. Popescu, L. Rosu, R. Trusca, I. Carcea, V. Soare, D. Dumitrescu, I. Constantin, M.T. Olaru and B.A. Carlan: IOP Conf. Series, 400, (2018) 022049.
23) T. Nagase, Y. Iijima, A. Matsugaki, K. Ameyama and T. Nakano: Mater. Sci. Eng. C **107** (2020) 110322.
24) V.T. Nguyen, M. Qian, Z. Shi, T. Song, L. Huang and J. Zou: Intermetallics **101** (2018) 39–43.
25) O.N. Senkov, G.B. Wilks, D.B. Miracle, C.P. Chuang and P.K. Liaw: Intermetallics **18** (2010) 1758–1765.
26) O.N. Senkov, G.B. Wilks, J.M. Scott and D.B. Miracle: Intermetallics **19** (2011) 698–706.
27) O.N. Senkov, J.M. Scotta, S.V. Senkova, D.B. Miracle and C.F. Woodward: J. Alloy. Compd. **509** (2011) 6043–6048.
28) O.N. Senkov, J.M. Scott, S.V. Senkova, F. Meisenkothen and D.B. Miracle: J. Mater. Sci. **47** (2012) 4062–4074.
29) O.N. Senkov, D.B. Miracle, K.J. Chaput and J.-P. Couzinie: J. Mater. Res. **33** (2018) 3092–3128.
30) T. Nagase, S. Anada, P.D. Rack, J.H. Noh, H. Yasuda, H. Mori and T. Egami: Intermetallics **38** (2013) 70–79.
31) T. Nagase, S. Anada, P.D. Rack, J.H. Noh, H. Yasuda, H. Mori and T. Egami: Intermetallics **26** (2012) 122–130.
32) Kennametal Stellite's team: http://www.stellite.com/en/home.html, (accessed, 24 September 2019).
33) T.M. Devine, F.J. Kummer and J. Wulff: J. Mater. Sci. **7** (1972) 126–128.
34) T.M. Devine and J. Wulff: J. Biomed. Mater. Res. **9** (1975) 151–167.
35) J. Cohen, R.M. Rose and J. Wulff: J. Biomed. Mater. Res. **12** (1978) 935–937.
36) T. Kilner, R.M. Pilliar, G.C. Weatherly and C. Alibert: J. Biomed. Mater. Res. **16** (1982) 63–79.
37) M. Niinomi: Metall. Mater. Trans. A **33** (2002) 477–486.
38) M. Niinomi, M. Nakai and J. Hieda: Acta Biomater. **8** (2012) 3888–3903.
39) M. Niinomi: J. Biomed. Mater. Res. A **107** (2019) 944–954.
40) ASTM F75, https://www.astm.org/Standards/F75, (accessed, 17 September 2018).
41) ASTM F1537-08, https://www.astm.org/Standards/F1537.htm, (accessed, 16 May 2019).
42) JIS T 7402, http://www.jisc.go.jp/eng/index.html, (accessed, 17 September 2018).
43) C.-Y. Hsu, C.-C. Juan, W.-R. Wang, T.-S. Sheu, J.-W. Yeh and S.-K. Chen: Mater. Sci. Eng. A **528** (2011) 3581–3588.
44) X. Yang and Y. Zhang: Mater. Chem. Phys. **132** (2012) 233–238.
45) A. Takeuchi and A. Inoue: Mater. Trans. **46** (2005) 2817–2829.
46) A. Jain, S.P. Ong, G. Hautier, W. Chen, W.D. Richards, S. Dacek, S. Cholia, D. Gunter, D. Skinner, G. Ceder and K.A. Persson: APL Materials, **1** (2013) 011002.
47) https://materialsproject.org/, (accessed, 23 August 2019).
48) T. Nagase, P.D. Rack, J.H. Noh and T. Egami: Intermetallics **59** (2015) 32–42.
49) T. Nagase, M. Suzuki and T. Tanaka: J. Alloy. Compd. **619** (2015) 267–274.
50) T. Nagase, M. Suzuki and T. Tanaka: Intermetallics **61** (2015) 56–65.
51) T. Nagase, M. Suzuki and T. Tanaka: J. Alloy. Compd. **619** (2015) 311–318.
52) T. Nagase and Y. Umakoshi: J. Alloy. Compd. **649** (2015) 1174–1181.
53) T. Nagase, M. Takemura, M. Matsumuro, M. Matsumoto and Y. Fujii: Mater. Des. **117** (2017) 338–345.
54) T. Nagase, T. Terai, T. Kakeshita, M. Matsumoto and Y. Fujii: Mater. Trans. **60** (2019) 554–560.
55) Materials Project, Ni$_3$Fe, ID: mp-1418, https://doi.org/10.17188/1190197.
56) C. Niu, A.J. Zaddach, A.A. Oni, X. Sang, J.W. Hurt, III, J.M. LeBeau, C.C. Koch and D.L. Irving: Appl. Phys. Lett. **106** (2015) 161906.
57) Materials Project, Fe$_9$Co$_7$, ID: mp-601842, https://doi.org/110.17188/1277337.
58) Materials Project, Mn$_2$CrCo, ID: mp-864955, https://doi.org/10.17188/1310273.
59) Materials Project, Co$_3$Mo, ID: mp-1139, https://doi.org/10.17188/1187793.
60) T. Nagase, A. Terayama, T. Nagaoka, N. Fuyama and T. Sakamoto: J. JFS **91** (2019) 717–729.
61) K.J. Laws, C. Crosby, A. Sridhar, P. Conway, L.S. Koloadin, M. Zhao, S. Aron-Dine and L.C. Bassman: J. Alloy. Compd. **650** (2015) 949–961.
62) T. Nagase, A. Shibata, M. Matsumuro, M. Takemura and S. Semboshi: Mater. Des. **181** (2019) 107900.
63) T. Nagase, M. Matsumoto and Y. Fujii: J. Alloy. Compd. **738** (2018) 440–447.
64) C.W. Bale, A.D. Pelton, W.T. Thompson and G. Eriksson: FactSage, Ecole Poly-technique, Montreal, http://www.factsage.com/, (accessed 16 September 2019).
65) P. Villars and K. Cenzual: Peason's crystal data - Crystal Structure Database for Inorganic Compounds, release December 2011, Materials Park, Ohio, U.S.
66) T. Nagase, M. Takemura, M. Matsumuro and T. Maruyama: Mater. Trans. **59** (2018) 255–264.
67) M.-H. Tsai, K.-Y. Tsai, C.-W. Tsai, C. Lee, C.-C. Juan and J.-W. Yeh: Mater. Res. Lett. **1** (2013) 207–212.
68) T. Nagase: Mater. Sci. Forum **941** (2018) 1238–1241.
69) U.S. Hsu, U.D. Hung, J.W. Yeh, S.K. Chen, Y.S. Huang and C.C. Yang: Mater. Sci. Eng. A **460–461** (2007) 403–408.
70) T. Nagase and Y. Umakoshi: J. Alloy. Compd. **650** (2015) 342–350.
71) T. Nagase, M. Suzuki and T. Tanaka: J. Alloy. Compd. **619** (2015) 332–337.
72) T. Nagase: Mater. Trans. **57** (2016) 156–162.
73) T. Nagase, T. Terai, T. Kakeshita and K. Morita: J. Soc. Mater. Sci., Japan **68** (2019) 205–211.